Preliminary results concerning the development of a water-propellant vaporizing liquid microthruster for small satellites

Maria Grazia De Giorgi*, Luca Francioso**, Chiara De Pascali**, Antonio Ficarella* and Donato Fontanarosa*
*Dept. of Engineering for Innovation, University of Salento, Via per Monteroni "Campus Ecotekne", LECCE I-73100, Italy
**Institute for Microelectronics and Microsystems IMM-CNR, Via per Monteroni "Campus Ecotekne", LECCE I-73100, Italy

Abstract

The recent advancement in microfabrication technologies has found application in academic, industrial and space programs aiming at the development of small satellites (total mass less than 20 kg). Thanks to the reduction of the total expenditure, space missions such as orbit transfer or formation flying have been extensively investigated, and actual results have shown the need for thrust forces from few μN up to some mN in combination with stringent constraints of mass, volume and power consumption limits. In this context, the micro-propulsion system represents a key technology, and Micro-Electric-Mechanical Systems (MEMS) based microthrusters have been demonstrated to be the most promising one.

The present work aims to develop a low-cost microresistojet for micro and nano-satellites orbit and/or attitude control. In particular, the paper reports the final design of a silicon-based water-propellant vaporizing liquid microthurster (VLM) prototype and some of the system engineering novelties faced during the development stage. The VLM composes of an inlet chamber, a set of parallel microchannels as heating chamber, and a planar convergent-divergent micronozzle. Different microchannel geometries and inlet chamber configurations have been designed in order to evaluate their impact on micro flow boiling instabilities. The microthruster has a sandwich structure. The inlet chamber, the heating chamber and the micronozzle have been fabricated using anisotropic wet etching of a silicon substrate coupled with specialty Borofloat 33® glass. The Borofloat wafer was coupled to silicon wafer by thermocompressive bonding, which allowed to ensure one optical access to the flow field inside the microthruster. The heating of the propellant is provided by means of a Platinum resistive heater placed on the bottom of the silicon die. In addition, a set of thermistors and vapor quality capacitive sensors have been designed to implement the microthruster with sensing capabilities for the flow instability control. Furthermore, secondary low-power platinum resistive heaters have been placed into the single channel volume for fine flow control by localized heating operation.

The operational feasibility of the microthruster has been assessed by means of a preliminary characterization, based on experimental tests supported by numerical investigations.

1. Introduction

The recent advancements in microfabrication technologies has allowed for the reduction of the total expenditure of space missions. Consequently, the efforts of the scientific community have gone into research and development of cubesats, namely micro-/ nano-satellites made of multiples of $10\times10\times10$ cm^3 cubic units with total mass less than 20 kg. These satellites are usually involved in missions which usually require small thrust forces from μN to some mN in compliance with stringent constraints of mass, volume and power consumption. Therefore, the micro-propulsion system represents a key technology [1]. As reported in [2], it should provide at the same time high velocity increments ΔV to allow for orbit transfer or long-time station keeping maneuvers and multi-axes thrust for wheel unloading in deep space or rendezvous of multiple satellites. In addition, the use of ultra-safe green propellants in place of the traditional toxic bi-/mono-propellants such as hydrazine, represents another relevant requirement for micro-propulsion system. In this regard, the ideal propellant should be in a condensed state at standard pressure and temperature and be completely harmless, which will also provide new usability for cubesats.

The last developments in microthruster technology have benefit from the advancement in Micro-Electric-Mechanical Systems (MEMS) machining. We refer to [3] for a detailed review of micro-propulsion systems applied to small satellites. In the field of the micro-propulsion, micro-resistojets represent an interesting choice since such electro-thermal micro-thrusters are currently able to provide thrust levels in the range 0.1-10 mN as required for the attitude

control and the pointing systems of miniaturized spacecrafts [4][5], while meeting all mass, volume and power constraints 6. The propellant is stored in the liquid or solid phase; thus, vaporization or sublimation is required prior to the heating of the gas. Devices that use liquid propellants are called Vaporizing Liquid Microthrusters (VLMs). Compared to cold/hot gas micro-thrusters, VLMs can store the propellant in low pressure and light weight fuel tank, but they will consume more electric power due to the evaporation process.

Mueller [7,8,9] first investigated a silicon-based MEMS device and investigated the heat losses in relation to the packaging and evaluated the influence of feeding pressure on the vaporization process. Similarly, Makherjee et al. [10] developed a MEMS-based micro-thruster by means of wet anisotropic etching. Water was used as propellant, and experiments showed thrust force magnitudes ranging between 0.15-0.46 mN. Instead, Maurya et al. [11] integrated micro-heater into a silicon-based VLM, which exhibited thrust forces in the range 5 to 20 µN with a heating power between 1 W and 2.4 W using water as propellant. Later, a single-channel VLM was manufactured and tested by Kundu et al. [12] which was equipped with two integrated heaters in order to provide a more uniform heating and a thrust force of 1 mN using maximum heater power of 3.6 W. Ye et al. [13] designed a different concept of VLM with pulsated heating by means of the application of an electric pulse. Their micro-thruster exhibited a total impulse of 0.2 µNs with pulse power of 30 W. More recently, Silva et al. 5 developed a new VLM with integrated molybdenum heaters and temperature sensing using water as green propellant, able to meet the strict requirements of the CubeSats and PocketQubes programs. Instead, Chen et al. [14] investigated the two-phase flow characteristics in a single channel silicon-based VLM, observing four different flow patterns, i.e. snake flow, vapor-droplet flow, vapor-droplet-jet flow and vapor flow. Concerning new materials and manufacturing technologies, Karthikeyan et al. [15] first developed a low temperature co-fired ceramic (LTCC) VLM, demonstrating that the LTC can replace the silicon, owing to good electrical conductivity of printed metallization, a relative low cost for mass production, and a relatively simple and fast fabrication process. Later, Cheah and Low [16] successfully tested a high temperature co-fired ceramic (HTCC) microthruster characterized by a three layers structure with a platinum-based microheater. The proposed ceramics-based VLM exhibited an improved specific impulse efficiency, as well as a reduction of the electrical power consumption in comparison to the silicon-based VLM.

The overall performance of the VLMs is usually affected by the establishment of micro-flow boiling instabilities inside the microchannels of the heating chamber. In this regard, Cen and Xu [17] fabricated a MEMS-based VLM made by parallel microchannels and performed a preliminary characterization the flow boiling instabilities in relation to the measured performance. Furthermore, the propulsive efficiency of this kind of microthrusters is also affected by both the growth of the viscous boundary layer inside planar micronozzles, enhanced by the micro-scale and the rarefied gas condition, as well as the expansion of non-equilibrium two-phase vapor flow into the micronozzle.

In this context, both the geometry optimization and embedded sensing capability play a crucial role in controlling the heating process and the behavior of the two-phase flow, so as to mitigate the efficiency losses and hinder the fluid-induced instabilities. The present work aims to present the design of a VLM concept which is equipped with temperature and void fraction sensors, and a secondary fine-heating system. Furthermore, the baseline configuration is made of parallel rectangular microchannels, yet several geometry modifications have been considered in order to reduce the flow boiling instabilities. Finally, preliminary tests have been carried on the first prototype of the device, which demonstrated the operational functioning of the overall microthruster as well as the integrated temperature and the void fraction sensors.

2. Device description

A 3D schematic of the vaporizing liquid microthruster is shown in Figure 1. It composes of three regions:
- an inlet chamber or plenum through which the propellant is fed;
- the heating chamber where the propellant is vaporized;
- a planar convergent-divergent micronozzle which accelerates the superheated vapor flow to supersonic velocities.

The VLM has a sandwich structure: the inlet chamber, the heating chamber and the micronozzle are realized by deep silicon anisotropic etching, coupled with a Borofloat 33® glass wafer that ensures fluidic tightness, optical access to the flow field inside the microthruster channels and sensor integration. The heat is provided to the propellant fluid by means of a thin film Platinum heater placed on the bottom of the silicon substrate.
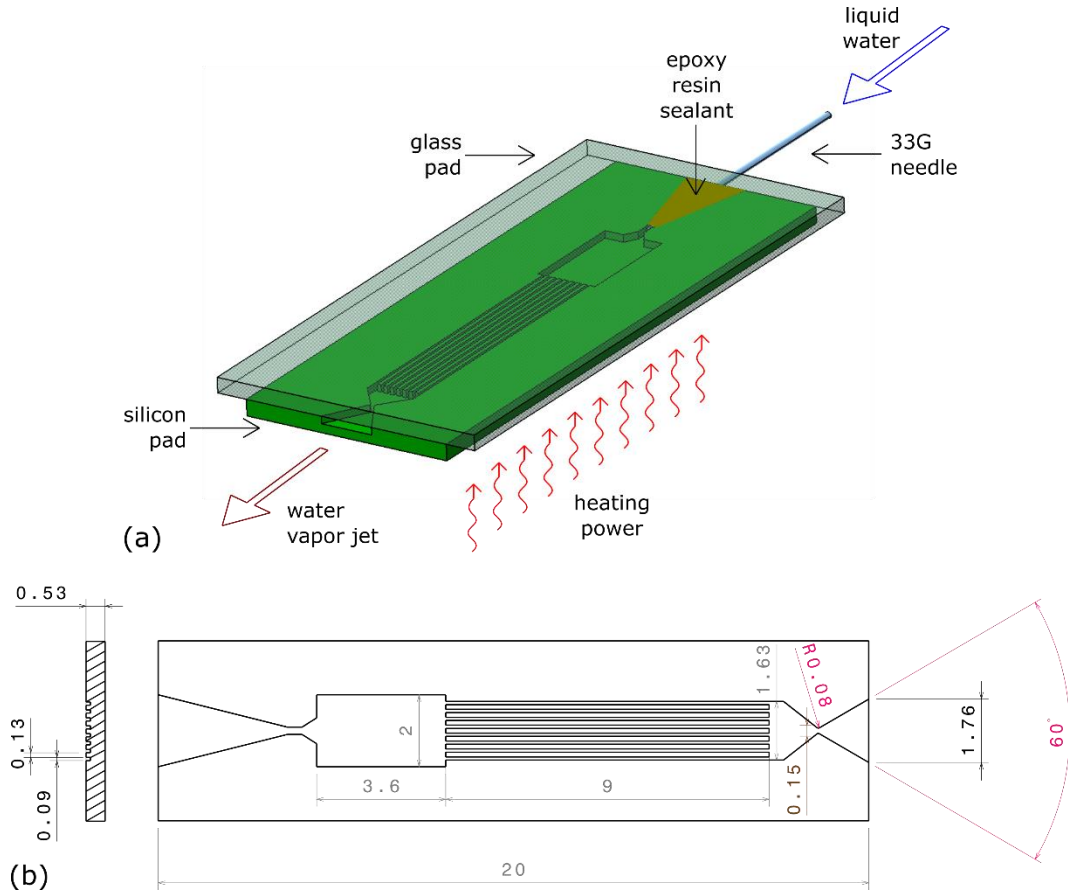
Figure 1: Concept of the vaporizing liquid microthruster: (a) 3D schematic view; (b) 2D drawing of the silicon pad (units are in millimetre).

The device has been equipped with a set of capacitive void fraction sensors (VFSs) and 4-wires resistance temperature detectors (RTDs), which aim to provide sensing capabilities for the control of the flow inside the microthruster. Furthermore, secondary resistive heaters have been patterned by photolithography on the glass substrate as low-power heating for flow control test. The MEMS schematics in Figure 2 highlights the configuration of sensors and heaters.

Concerning the microthruster dimensions, the geometry of the thruster device has length of about 20 mm, width of 7 mm and total thickness of about 500 μm, while the etching depth for channel definition is about 230 μm. The glass layer has the same length of the silicon substrate, it has a thickness of about 500 μm and 9 mm width in order to allow placement of the connection pads and secondary heaters the electrical pads of sensors and secondary heaters. A V-shaped inlet of about 2 mm length ensures water feeding inside the chip with a 33G needle, which is glued to the device using an epoxy resin that provides the proper junction tightness. The heating chamber is made of eight microchannels of 90 μm width and 9 mm length, which should ensure the maximization of the heat transfer coefficient, the reduction of the pressure losses and the control of flow boiling instabilities. Microchannels are spaced apart of 130 μm each other, The micronozzle has a throat width of about 150 μm, the convergence angle is about 45°, while the divergent section owns 30° respectively. The choice of a high divergence angle is related to the mitigation of the viscous losses due to the boundary layer growth normal to the planar walls, whose negative impact on micronozzle performance strongly increases with the length of the divergent section as demonstrated in [18].
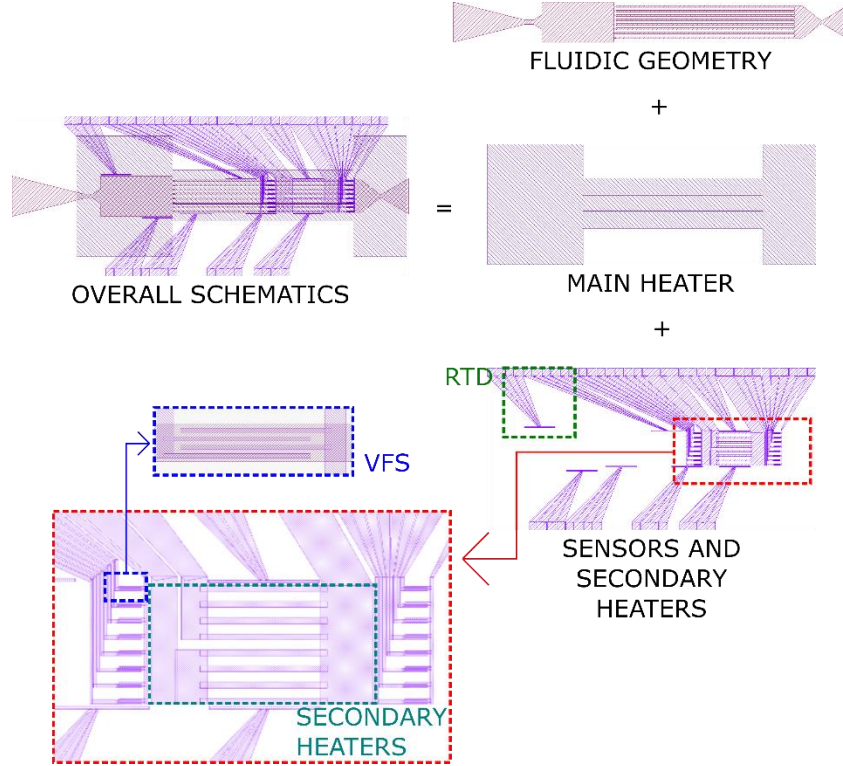
Figure 2: MEMS schematics of the microthruster.

Concerning the propellant selection, it results from a trade-off between performance, safety, and any other desired features such as density, heat capacity, safety, storability and availability. Based on the analysis performed by [19] water has been selected as the propellant for use in the present VLM. In fact, they performed a deep analysis on several fluids considering four parameters for comparison: the increment of velocity per unit volume ΔV/V, the specific impulse I_{sp}, the electrical power needed for vaporization $P_{el,v}$, and the safety issue. They found that water can accelerate the spacecraft to higher velocities using the same volume of propellant thanks to the high ΔV/V. In addition, water ensures safe operational environment, it is environmentally friendly and cheap, it has high density and it is stable enough to be stored in a weakly pressurized light tank. The drawback is greater power consumption due to the high enthalpy of vaporization, yet it can still meet the expected requirements for small satellites.

3. Numerical predictive analysis

The one-dimensional model of the VLM, which was proposed and validated by the authors in [20], has been applied to the present configuration. It allows to describe the behaviour of the liquid–vapor flow inside the inlet and the heating chambers of the microthruster, based on the hypothesis of thin film flow and considering the 1D approximation [21], which give the following simplifications:
- the fluid is Newtonian;
- the fluid properties are averaged over both the height and the width of the flow;
- no slip condition between fluid and walls;
- inertia and other body forces such as the gravity, are supposed negligible compared to pressure and viscous forces, so that the velocity changes result instantaneous.

The heating process begins into the inlet chamber at the end of which the flow enters the microchannels region. The toolbox CoolProp [22] is integrated into the code to compute the two-phase mixture properties, which are averaged by supposing the homogeneous mixture of liquid and vapor in thermodynamic equilibrium.

The resulting set of governing equations are represented by Eqs. (1), (2) and (3), which respectively describe the balance of mass, momentum and energy at each grid step Δs, as follows:

$$\dot{m} = \rho_m u A_{cs} \tag{1}$$

$$\Delta P = -u \frac{12\mu_m}{Z_{ch}^2} \Delta s \tag{2}$$

$$\Delta H = \dot{Q} \Delta t = \dot{q} P_{cs} \Delta s = [h_b(T_w - T)] P_{cs} \Delta s \tag{3}$$

In the equations above, the time step is Δt, ΔH is variation of the total enthalpy of the flow, ρ_m and μ_m are the density and the dynamic viscosity of the mixture, while Z_{ch} is the height of the channels, which also corresponds to the depth of the entire thruster. Moreover, A_{cs} is the area of the cross section, $\dot{Q}$ is the heat power exchanged between the fluid and the silicon walls and P_{cs} is the perimeter of the cross section. The heat flux $\dot{q}$ is related to the convective heat exchange driven by the heat transfer coefficient $h_b = Nu \, (\kappa_{cond}/D_h)$, where κ_{cond} is the local thermal conductivity coefficient of the fluid and D_h is the hydraulic diameter. Instead, the Nusselt number Nu is locally estimated based on the empirical correlations extrapolated by Tibiriçá et al. [23].

As a result, the local heat transfer coefficient is estimated as in Eq. (4):

$$h_b = \begin{cases} \frac{Nu(x) \, \kappa_{cond}}{D_h}, & x < x_{d/o} \\ \frac{Nu(x) \, \kappa_{cond}}{D_h} - 0.5 \left[\frac{Nu(x) \, \kappa_{cond}}{D_h} - h_{b,DB} \right] \frac{(x - x_{d/o})}{(1 - x_{d/o})}, & x \geq x_{d/o} \end{cases} \tag{4}$$

where $x_{d/o}$ represents the vapor quality at the dry-out condition, while the local Nusselt number and the Dittus–Boelter super-heated vapor relation are defined in Eqs. (5) and (6):

$$Nu(x) = \begin{cases} 0.68 \, Pr^{0.5414} \, La^{0.1942} \, Re^{0.5873} (1-x)^{-0.2446} \, Bo^{0.3544}, & x < x_{d/o} \\ 0.68 \, Pr^{0.5414} \, La^{0.1942} \, Re^{0.5873} (1-x_{d/o})^{-0.2446} \, Bo^{0.3544}, & x \geq x_{d/o} \end{cases} \tag{5}$$

$$h_{b,DB} = 0.023 \, \frac{\kappa_{v,cond}}{D_h} Re_v^{0.8} \, Pr_v^{1/3} \tag{6}$$

In equations above, Re_v and Pr_v respectively are the local Reynolds and Prandtl numbers of the vapor phase.

The prediction of the microthruster performance in terms of thrust and specific impulse is based on the ideal rocket theory (IRT). By supposing chocked flow conditions at the throat section of the micronozzle, the maximum mass flow rate $\dot{m}_{IRT}$ and the exhaust velocity are expressed as a function of the stagnation pressure p_0, temperature T_0 at the exit of microchannels, the static pressure at the exit section p_{exit} and the area at the throat section A^*, as follows:

$$\dot{m}_{IRT} = \Gamma_{VDK} \frac{p_0 A^*}{\sqrt{R_{gas} T_0}} \tag{7}$$

$$u_{exit,IRT} = \sqrt{\frac{2\gamma R_{gas} T_0}{\gamma - 1} \left[1 - \left(\frac{p_{exit}}{p_0} \right)^{\frac{\gamma-1}{\gamma}} \right]} \tag{8}$$

where R_{gas} is specific gas constant, $\Gamma_{VDK} = \left[\gamma \left(2/\gamma - 1 \right)^{\frac{(\gamma+1)}{(\gamma-1)}} \right]^{1/2}$ is the Vanderkerchoff factor, γ is the specific heat ratio of the propellant. Therefore, the thrust and the specific impulse result from Eqs. (9) and (10),

$$F_{IRT} = F_{j,IRT} + F_{p,IRT} = \dot{m}_{IRT} u_{exit,IRT} + (p_{exit} - p_{amb}) A_{exit} \tag{9}$$

$$I_{sp,IRT} = \frac{F_{IRT}}{\dot{m}_{IRT} g_0} = \frac{u_{eff}}{g_0} \tag{10}$$

where the subscripts j and p denote the momentum thrust and the pressure thrust respectively, and u_{eff} is the effective exhaust velocity which takes into account both thrust terms, p_{amb} is the farfield ambient pressure.

The establishment of the boundary layer at the nozzle throat and along the divergent section of the micronozzle reduces both the mass flow rate and the exit velocity. Hence, the micronozzle quality ξ_n has been considered in order to quantifies the total performance losses due to growth of the the boundary layer thickness inside the micronozzle as follows:

$$F_{act} = \dot{m}_{act} u_{act} = (C_d \dot{m}_{IRT}) + (\eta_u u_{exit,IRT}) = (C_d \eta_u) \dot{m}_{IRT} u_{exit,IRT} = \xi_n F_{IRT} \tag{11}$$

where the subscript act denotes the actual performance, C_d is the discharge coefficient and η_u is the Isp-efficiency, In particular, C_d is related to the geometry of the nozzle throat, the propellant and the Reynolds number at the throat section, while η_u depends on both the compressible momentum and the displacement thicknesses as a measure of the the jet momentum reduction due to the difference between the inviscid and the viscous velocity inside the boundary layer. We refer to [20] for the detailed description of the model and for the operational range of validity of the experimental correlations regarding the two-phase flow behavior.

4. Microthruster fabrication

The microthrusters fabrication has been performed at the CNR-IMM clean room facilities, with a custom process design that integrates different pattern transfer techniques, vacuum depositions, deep dry etching of silicon, front-back lithography alignment steps and adhesive silicon-glass bonding. The process starts from DSP (100) p-type silicon wafers, 4" diameter and Borofloat 33® 4" wafers, both 500 microns thick. The first lithography step was performed to define the platinum structures (heaters, RTD and VFS sensors) adopting a 365 nm UV lithography with AZ5214 reversal tone resist; wafers with patterned photoresists were loaded into an RF sputtering tool for the deposition of 10 nm of titanium as adhesion layer followed by 500 nm of platinum. Subsequently the lift-off step in acetone removed the unwanted metal and the glass wafer was spin-coated again with a high temperature resistant photodefinable Perminex 1000 polymer for glass/silicon adhesive bonding. The Perminex layer, about 13 µm thick has been patternen by a second lithography step and developed into dedicated developed supplied by MicroChem company. The soluble Perminex layer was removed onto unwanted areas related to channels, plenum and nozzles; wafers then stored for final alignment and bonding step. The second fabrication step was related to realization of main heaters on backside of polished silicon wafer, by a photolithography step and 10/500 nm Ti/Pt deposition by RF sputtering. The third phase of fabrication was related to deep anisotropic etching of silicon, performed by a dedicated lithography step with photoresist mask. The wafers with patterned resist mask were loaded into a STM ICP dry etcher for deep anisotropic etching of silicon by Bosch process in SF_6/O_2 gas mixture. After an etching step of about 230 microns depth, the wafers were cleaned form resist masks and loaded into the PECVD reactor for the deposition of a SiO_2 passivation layer of about 1 µm. This layer allows the electrical insulation inside the different channels and avoid the semiconductor silicon substrate to modify the sensors data acquisition. After the preparation of glass and silicon wafers, the wafers were diced into singles microthrusters and the silicon and glass substrates coupled and aligned with optical microscope to perform the thermocompressive final bonding step. This process has been performed on a commercial bonding tool at 150 °C for 10 minutes and 300 Kg/cm^2 applied load.

A picture of a microthruster prototype is shown in Figure 3 (a), while Figure 3 (b) displays the front and side views of the microthruster in its operative configuration with both feeding needle and electrical wirings of the main heater.
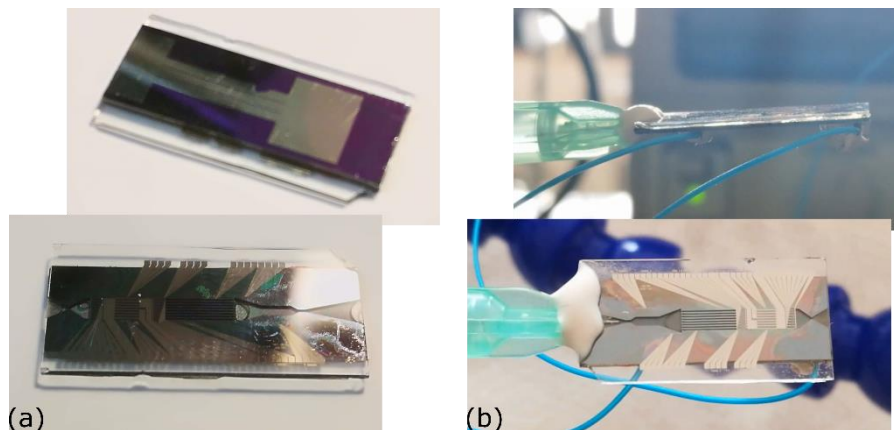

Figure 3: Picture of a VLM prototype: (a) top and bottom views of the manufactured device; (b) top and side views of the operative configuration equipped with the feeding needle and the electrical wire of the main heater.

5. Operational characterization

5.1 Experimental study

A custom experimental setup has been implemented for the characterization of the different sensors and actuators embedded into the microthruster. To this aim, different tests have been carried out to generate reliable calibration curve for the RTD sensors (for real temperature detection on chip), the main heater (for heating of the chamber and channels by Joule effect) and the capacitive void fraction sensors (VFSs) for vapour/liquid ratio identification.

The set of experiments reported in Table 1 was planned for a complete analysis of the device properties. Three mass flow rates were considered, and flow observation, pressure and temperature measurements have been performed using the RTD placed close to the micronozzle, considering that the density of water at ambient condition is about 998.2 kg/m^3. The experimental results for RTD without (empty configuration, at $\dot{m}$=0 kg/s) and with water flow (propulsive configuration) are reported below.

Table 1. Test Matrix

Test case #	$\dot{m}$ [kg/s]^a	V_{app} [V]	T_{water} [K]	P_0 [Pa]	T_{exit} [K]	P_{el} [W]
MRF12p5_1V	3.47×10^{-6}	1	296.15	1.36×10^5	312.09	0.53
MRF12p5_2V	3.47×10^{-6}	2	296.15	1.36×10^5	351.54	2.02
MRF12p5_3V	3.47×10^{-6}	3	296.15	1.34×10^5	387.19	4.26
MRF12p5_4V	3.47×10^{-6}	4	296.15	1.33×10^5	389.16	7.44
MRF12p5_5V	3.47×10^{-6}	5	296.15	1.34×10^5	392.45	11.50
MRF12p5_6V	3.47×10^{-6}	6	296.15	1.41×10^5	397.16	15.36
MRF12p5_7V	3.47×10^{-6}	7	296.15	1.52×10^5	563.01	18.62
MRF18_1V	4.99×10^{-6}	1	296.15	1.52×10^5	313.15	0.57
MRF18_2V	4.99×10^{-6}	2	296.15	1.51×10^5	343.13	2.06
MRF18_3V	4.99×10^{-6}	3	296.15	1.50×10^5	382.58	4.26
MRF18_4V	4.99×10^{-6}	4	296.15	1.48×10^5	387.9	7.40
MRF18_5V	4.99×10^{-6}	5	296.15	1.50×10^5	389.57	11.55
MRF18_6V	4.99×10^{-6}	6	296.15	1.53×10^5	394.53	16.08
MRF18_7V	4.99×10^{-6}	7	296.15	1.60×10^5	402.23	21.35
MRF24_1V	6.65×10^{-6}	1	296.15	1.69×10^5	313.00	0.56
MRF24_2V	6.65×10^{-6}	2	296.15	1.69×10^5	340.30	2.06
MRF24_3V	6.65×10^{-6}	3	296.15	1.69×10^5	377.52	4.38
MRF24_4V	6.65×10^{-6}	4	296.15	1.67×10^5	387.59	7.44
MRF24_5V	6.65×10^{-6}	5	296.15	1.65×10^5	389.26	11.4
MRF24_6V	6.65×10^{-6}	6	296.15	1.70×10^5	393.67	16.20
MRF24_7V	6.65×10^{-6}	7	296.15	1.81×10^5	397.52	21.49

^{a} estimated by considering constant water density ρ_{water}=998.2 kg/m^3

Figure 4 (a) reports the calibration of the RTD into a reference furnaces and the correlation between the experimental data (red cross) and the interpolation law. Once obtained this calibration for the RTD embedded into the devices, an experimental session has been focused on the collection of the vapour stream temperature vs the applied power to the main heater of the microthruster. As shown in Figure 4 (b), the applied voltage was correlated to an increasing Joule heating of the chip. The chip temperature increases as the power increase and a temperature plateau was recorded around 387 K. Further power increase caused a temperature spike and a rapid decrease to a stable value of about 400 K.
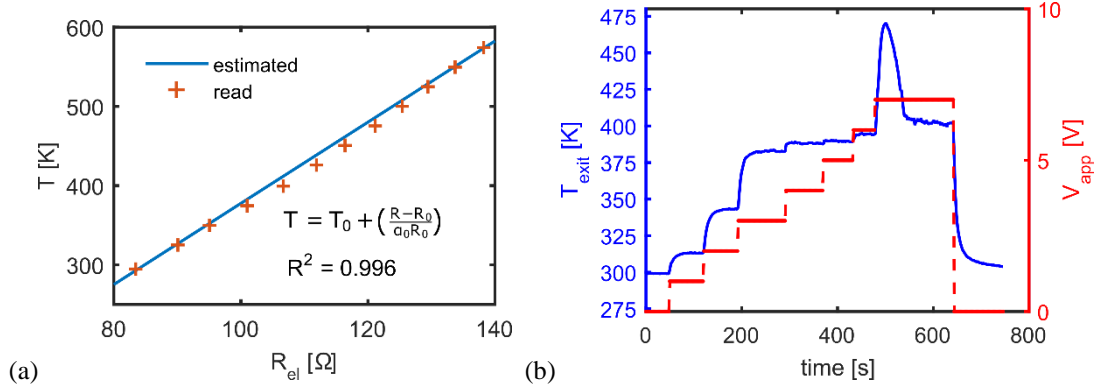
Figure 4: RTD characterization: (a) RTD calibration in the empty configuration at ṁ=0 kg/s (α_0=0.002337, R_0=83.51 Ω, T_0=293.15 K); (b) RTD temperature measurement during 0-7 volts loading cycle in operative configuration at ṁ=4.99 × 10^{-6} kg/s (α_0=0.002337, R_0=84.5 Ω, T_0=297.15 K).

In order to assess the validity of the measurement provided by the embedded RTD, the temperature of the microthruster was measured by means of a commercial thermistor (model PT1000) secured at the midpoint on the bottom side of the microthruster, at mass flow rate of 3.47 × 10^{-6} kg/s and different electrical powers. Temperature readings resulted from resistance-temperature conversion relationship in accordance with the standard IEC751/ITS-90. The measured data were compared with ones provided by the integrated RTD at the same mass flow rate (test cases MRF12p5_1V to MFR12p5_7V), as shown in Figure 5. Even though the temperature measure provided by the embedded RTD was higher than those read through the sensor PT1000 (due to some thermal resistance at the interface between PT1000 sensors and chip surface), the two experimentally retrieved curve exhibited the same trend with good data fit. This result confirmed the reliability of the temperature sensing provided to the VLM by the integrated RTD.
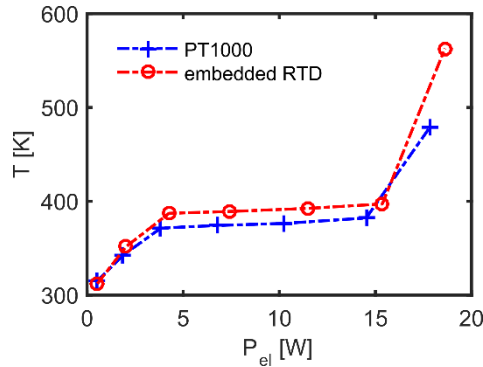

Figure 5: Temperature measurement provided by the integrated RTD (red line with circles) in comparison with the one provided by the sensor PT1000 (blue line with crosses).

5.2 Numerical performance prediction

As evinced from the experimental data reported in Table 1, full evaporation with significant superheating of the vapor flow inside the microchannel was retrieved at mass flow rate of 3.47 × 10^{-6} kg/s and electrical power of 18.62 W (test case MRF12p5_7V). Hence, based on the temperature and pressure measurement, a preliminary estimation of the performance of the microthruster under vacuum condition was performed using the one-dimensional modeling previously described. In particular, the feeding pressure and the wall temperature were set to 1.52 × 10^5 Pa and 563.01 K, respectively, while water temperature at the microthruster entrance was assumed equal to 296.15 K. The far field pressure downstream the microthruster was supposed equal to 20 Pa. The solution of the two-phase flow inside the inlet chamber and microchannels is reported in Figure 6. Numerical prediction confirmed the complete evaporation of the flow, which would enter the micronozzle at a temperature of about 464 K and a total pressure of about 1.51 × 10^5 Pascal.
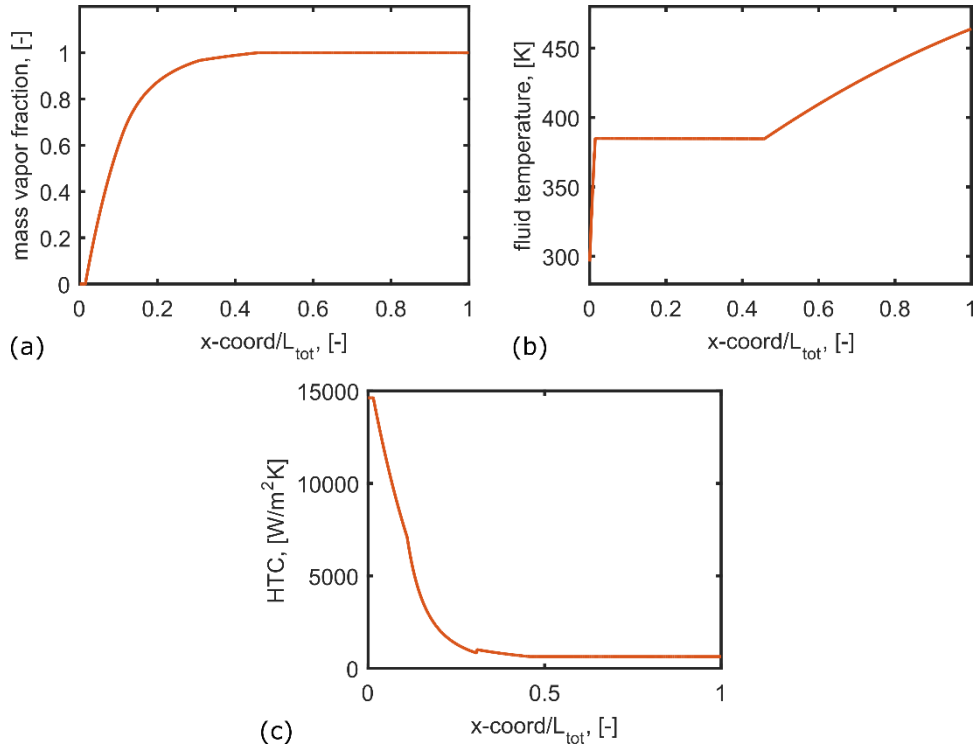
Figure 6. One-dimensional numerical prediction of the two-phase flow behavior inside the heating region (inlet chamber and microchannels): (a) vapor quality; (b) fluid temperature; (c) heat transfer coefficient (HTC). L_{tot} is the length of the heating region.

Based on the micronozzle inlet conditions estimated at the exit of the microchannels, the solution of the supersonic expansion was given. As a result, the mass flow rate should be increased to about 7.17×10^{-6} kg/s in order to ensure the chocked flow condition at the throat section. Computations estimated a micronozzle quality ξ_n of 0.87 approximately. Therefore, the predicted net thrust would be about 7.7 mN, corresponding to a specific impulse of about 110 s.

6. Conclusions

The present work presented the development of a wafer-level fabrication of a micro-resistojet for micro and nano-satellites orbit and/or attitude control. In particular, the design and the fabrication of a silicon/glass water-propellant vaporizing liquid microthurster (VLM) was reported. The experimental characterization confirmed the functionality of the devices with different sets of experiments, at mass flow rate of 3.47×10^{-6} kg/s and different supplied powers for Joule effect heating of the chip. The embedded RTD have been tested and compared with commercial PT1000 thin film miniature sensors with a good agreement of measured temperature near the VLM channels between the two sensors. The embedded sensors for temperature and capacitive void fraction detection will enable a real time state-of-the-art control on vaporizing efficiency and stream optimization for each single channel. Experimental test confirmed that the full evaporation with significant superheating of the vapor flow inside the microchannel was retrieved at mass flow rate of 3.47×10^{-6} kg/s and electrical power of 18.62 W. A preliminary estimation of the performance of the microthruster under vacuum condition was performed using the one-dimensional modelling, obtaining a micronozzle quality of 0.87 and a predicted net thrust of about 7.7 mN, corresponding to a specific impulse of about 110 s.

References

1. C. Saaj, V. Lappas, H. Schaub, D. Izzo, Hybrid propulsion system for formation flying using electrostatic forces, Aerosp. Sci. Technol. 14(5) (2010) 348–355, https://doi.org /10.1016 /j.ast .2010.02.009.
2. Koizumi, H., Asakawa, J., Nakagawa, Y., Nishii, K., Takao, Y., Nakano, M., & Funase, R. (2019). Assessment of Micropropulsion System Unifying Water Ion Thrusters and Water Resistojet Thrusters. Journal of Spacecraft and Rockets, 1-9. https://doi.org/10.2514/1.A34407.
3. M. Silva, D. Guerrieri, A. Cervone, E. Gill, A review of MEMS micropropulsion technologies for cubesats and pocketqubes, Acta Astronaut. 143 (2018) 234–243, https://doi.org /10.1016 /j.actaastro .2017.11.049.
4. Y. Gao, Y.F. Ma, J.T. Liu, A review of the vaporizing liquid microthruster technology, in: 2014 ISFMFE – 6th International Symposium on Fluid Machinery and Fluid Engineering, 2014, pp.1–3.
5. M. Silva, D. Guerrieri, H. van Zeijl, A. Cervone, E. Gill, Vaporizing liquid microthrusters with integrated heaters and temperature measurement, Sens. Actuators A, Phys. 265 (2017) 261–274.
6. K. Lemmer, Propulsion for cubesats, Acta Astronaut. 134 (2017) 231–243, https://doi.org/10.1016/j.actaastro.2017.01.048.
7. J. Mueller, W. Tang, A. Wallace, R. Lawton, W. Li, D. Bame, I. Chakraborty, Design, analysis and fabrication of a vaporizing liquid microthruster, in: 33rd Joint Propulsion Conference and Exhibit, 1997, p.3054.
8. J. Mueller, D. Bame, I. Chakraborty, A. Wallace, W. Tang, R. Lawton, Proof-of-concept demonstration of a vaporizing liquid micro-thruster, in: 34th AIAA/ASME/SAE/ASEE Joint Propulsion Conference and Exhibit, 1998, p.3924.
9. J. Mueller, I. Chakraborty, D. Bame, W. Tang, Vaporizing liquid microthruster concept : preliminary results of initial feasibility studies, in: Micropropulsion for Small Spacecraft, Reston, VA, American Institute of Aeronautics and Astronautics, Inc., Prog. Astronaut. Aeronaut. 187 (2000) 215–230.
10. E. Mukerjee, A. Wallace, K. Yan, D. Howard, R. Smith, S. Collins, Vaporizing liquid microthruster, Sens. Actuators A, Phys. 83(1) (2000) 231–236, https://doi.org /10 .1016 /S0924 -4247(99)00389-1.
11. D. Maurya, S. Das, S. Lahiri, Silicon MEMS vaporizing liquid microthruster with internal microheater, J. Micromech. Microeng. 15(5) (2005) 966.
12. P. Kundu, T.K. Bhattacharyya, S. Das, Design, fabrication and performance evaluation of a vaporizing liquid microthruster, J. Micromech. Microeng. 22(2) (2012) 025016.
13. X. Ye, F. Tang, H. Ding, Z. Zhou, Study of a vaporizing water microthruster, Sens. Actuators A, Phys. 89(1–2) (2001) 159–165.
14. C.-C. Chen, C.-W. Liu, H.-C. Kan, L.-H. Hu, G.-S. Chang, M.-C. Cheng, B.-T. Dai, Simulation and experiment research on vaporizing liquid micro-thruster, Sens. Actuators A, Phys. 157(1) (2010) 140–149.
15. K. Karthikeyan, S. Chou, L. Khoong, Y. Tan, C. Lu, W. Yang, Low temperature co-fired ceramic vaporizing liquid microthruster for microspacecraft applications, Appl. Energy 97 (2012) 577–583.
16. K. Cheah, K.-S. Low, Fabrication and performance evaluation of a high temperature co-fired ceramic vaporizing liquid microthruster, J. Micromech. Microeng. 25(1) (2015) 015013.
17. J. Cen, J. Xu, Performance evaluation and flow visualization of a MEMS based vaporizing liquid micro-thruster, Acta Astronaut. 67(3–4) (2010) 468–482, https://doi .org /10.1016 /j.actaastro.2010.04.009.
18. M.G. De Giorgi, D. Fontanarosa, A. Ficarella, Modeling viscous effects on boundary layer of rarefied gas flows inside micronozzles in the slip regime condition, Energy Proc. 148 (2018) 838–845.
19. Guerrieri, D. C., Silva, M. A., Cervone, A., & Gill, E. (2017). Selection and characterization of green propellants for micro-resistojets. Journal of Heat Transfer, 139(10), 102001.
20. M.G. De Giorgi, D. Fontanarosa, A novel quasi-one-dimensional model for performance estimation of a Vaporizing Liquid Microthruster, Aerospace Science and Technology, Volume 84, 2019, Pages 1020-1034, ISSN 1270-9638, https://doi.org/10.1016/j.ast.2018.11.039.
21. G.P. Sutton, O. Biblarz, Rocket Propulsion Elements, John Wiley & Sons, 2016.
22. I.H. Bell, J. Wronski, S. Quoilin, V. Lemort, Pure and pseudo-pure fluid ther-mophysical property evaluation and the open-source thermophysical prop-erty library CoolProp, Ind. Eng. Chem. Res. 53(6) (2014) 2498–2508, https://doi .org /10 .1021 /ie4033999.
23. C. Tibiriçá, D. Rocha, I.L.S. Sueth Jr., G. Bochio, G. Shimizu, M. Barbosa, S. Fer-reira, A complete set of simple and optimized correlations for microchannel flow boiling and two-phase flow applications, Appl. Therm. Eng. 126 (2017) 774–795, https://doi .org /10 .1016 /j .applthermaleng .2017.07.161.